

RESEARCH ARTICLE

10.1002/2017JD026809

Key Points:

- Föhn winds in the lee of the Antarctic Peninsula mountains and their impacts are captured in high-resolution atmospheric model simulations and observations
- Significant changes in modeled components of the surface energy balance (SEB) occur during föhn
- The modeled response of net SEB and surface melt to föhn is not as strong as that seen in observations

Supporting Information:

- Supporting Information S1

Correspondence to:

J. C. King,
jcki@bas.ac.uk

Citation:

King, J. C., Kirchgaessner, A., Bevan, S., Elvidge, A. D., Kuipers Munneke, P., Luckman, A., Orr, A., Renfrew, I. A., & van den Broeke, M. R. (2017). The impact of föhn winds on surface energy balance during the 2010–2011 melt season over Larsen C Ice Shelf, Antarctica. *Journal of Geophysical Research: Atmospheres*, 122, 12,062–12,076. <https://doi.org/10.1002/2017JD026809>

Received 20 MAR 2017

Accepted 28 SEP 2017

Accepted article online 4 OCT 2017

Published online 17 NOV 2017

The Impact of Föhn Winds on Surface Energy Balance During the 2010–2011 Melt Season Over Larsen C Ice Shelf, Antarctica

J. C. King¹ , A. Kirchgaessner¹ , S. Bevan² , A. D. Elvidge³, P. Kuipers Munneke⁴ , A. Luckman² , A. Orr¹ , I. A. Renfrew³ , and M. R. van den Broeke⁴

¹British Antarctic Survey, Cambridge, UK, ²Department of Geography, Swansea University, Swansea, UK, ³School of Environmental Sciences, University of East Anglia, Norwich, UK, ⁴Institute for Marine and Atmospheric research Utrecht, Utrecht University, Utrecht, Netherlands

Abstract We use model data from the Antarctic Mesoscale Prediction System (AMPS), measurements from automatic weather stations and satellite observations to investigate the association between surface energy balance (SEB), surface melt, and the occurrence of föhn winds over Larsen C Ice Shelf (Antarctic Peninsula) over the period November 2010 to March 2011. Föhn conditions occurred for over 20% of the time during this period and are associated with increased air temperatures and decreased relative humidity (relative to nonföhn conditions) over the western part of the ice shelf. During föhn conditions, the downward turbulent flux of sensible heat and the downwelling shortwave radiation both increase. However, in AMPS, these warming tendencies are largely balanced by an increase in upward latent heat flux and a decrease in downwelling longwave radiation so the impact of föhn on the modeled net SEB is small. This balance is highly sensitive to the representation of surface energy fluxes in the model, and limited validation data suggest that AMPS may underestimate the sensitivity of SEB and melt to föhn. There is broad agreement on the spatial pattern of melt between the model and satellite observations but disagreement in the frequency with which melt occurs. Satellite observations indicate localized regions of persistent melt along the foot of the Antarctic Peninsula mountains which are not simulated by the model. Furthermore, melt is observed to persist in these regions during extended periods when föhn does not occur, suggesting that other factors may be important in controlling melt in these regions.

1. Introduction

In recent decades the Antarctic Peninsula (AP) has warmed more rapidly than almost any other region on Earth (Turner et al., 2005). Although the rate of warming has reduced since the mid-1990s (Turner et al., 2016), there have been major and rapid changes in the regional cryosphere including the retreat and breakup of the Larsen A and Larsen B ice shelves to the east of the AP (Cook & Vaughan, 2012). It is generally believed that the major driver of ice shelf retreat in this region is increased meltwater production in response to rising regional air temperatures (Scambos et al., 2000; van den Broeke, 2005). The rate of discharge of grounded ice from the AP has increased following the loss of the ice shelves (Rignot et al., 2004), implying an increased contribution to sea level rise from this region (Harig & Simons, 2015). The stability of Larsen C, the remaining ice shelf to the east of the AP, is currently uncertain (e.g., Jansen et al., 2015). Consequently, it is crucial to understand how this ice shelf may respond to future climate change in order to make predictions of the potential contribution of the AP to future sea level rise.

Analysis of instrumental and proxy climate records from the east coast of the AP has indicated that summer air temperatures in this region are strongly correlated with, and are very sensitive to, the strength of the prevailing circumpolar westerly winds (Abram et al., 2011; Marshall et al., 2006). In contrast, climate records from the west coast of the Peninsula show much weaker correlations with the strength of the westerlies. Marshall et al. (2006) suggested that this asymmetric sensitivity to changes in the strength of the westerlies arises as a result of the east coast of the AP being influenced by warm, downslope föhn winds in the lee of the AP mountains during periods of westerly flow. Simulations of episodes of westerly flow over the AP using high-resolution atmospheric models, validated with observations from instrumented aircraft, have confirmed the existence of föhn winds in this region and have demonstrated their impact on surface conditions over Larsen C Ice Shelf (Elvidge et al., 2015, 2016; Grosvenor et al., 2014; King et al., 2008). However, these

studies have been limited to just a few cases. In order to understand the climatological impact of föhn winds on melt rates over Larsen C Ice Shelf (LCIS), it is necessary to examine at least a whole melt season. The climatological impact of föhn winds on the (now disappeared) Larsen A and Larsen B ice shelves was recently investigated by Cape et al. (2015), who found strong correlations between the frequency of occurrence of föhn events and both near-surface air temperatures and the frequency of occurrence of surface melt in these regions. In the present paper we use a similar approach but focus on the more southerly LCIS and the 2010–2011 melt season.

In situ observations of melt rates are only available from a very limited number of locations on LCIS (Kuipers Munneke et al., 2012), but spatial patterns of seasonal melt have been retrieved from satellite-borne measurements using microwave radiometers (Tedesco, 2009) and radars (Barrand et al., 2013; Luckman et al., 2014) and have also been inferred from estimates of firn air content derived from airborne radar surveys (Holland et al., 2011). All of these remote sensing techniques reveal similar spatial patterns in the frequency of occurrence of melt over LCIS which have been confirmed by in situ observations of ice fabric structure (Ashmore et al., 2017). Melt frequency over the ice shelf decreases from north to south (consistent with regional climatological temperature gradients) and from west to east, with some of the highest melt frequencies seen in a narrow band running along the foot of the AP mountains at the western extremity of the ice shelf. This strongly resembles the spatial pattern of surface warming associated with föhn winds seen in case studies (Elvidge et al., 2016; Grosvenor et al., 2014) and thus suggests that föhn winds shape the spatial distribution of surface melt on this ice shelf.

In order to investigate this hypothesis, we have made use of data from an atmospheric model with 5 km horizontal grid spacing that was run for the whole of the 2010–2011 melt season (defined as November 2010 to March 2011). In section 2 below, we describe the model and validation data used and give details of the calculation of surface energy balance and melt diagnostics from the model output. We also describe how we use model output to detect the occurrence of föhn conditions. In section 3 we examine how surface energy balance and melt differ between föhn and nonföhn conditions using both model data and observations of surface melt derived from remote sensing. Finally, in section 4 we use our findings to develop an understanding of the role played by föhn winds in controlling the spatial and temporal variation of surface melt on LCIS.

2. Data and Methods

2.1. The Study Area

LCIS occupies a large embayment on the east side of the AP and extends from the Jason Peninsula at around 66°S to the Gipps Ice Rise at around 68.5°S (Figure 1). The shelf ice has an average thickness of around 240 m and, in 2005, covered an area of around 50,000 km². To the west, the ice shelf is bounded by the mountains of the AP, which rise to an average elevation of around 1,600 m between 66°S and 69°S but reach just over 2,000 m in the northern part of this region. LCIS is fed by tributary glaciers draining down the steep eastern face of the mountains into inlets at the western extremity of the ice shelf.

Although generally only 50 km wide, the high mountain ridge provides an effective barrier to the prevailing winds to the west of the AP that bring relatively warm maritime air from the west and northwest. As a result, annual mean temperatures over LCIS are 8–10°C lower than those at similar latitudes on the west coast of the AP (Morris & Vaughan, 2003). However, on occasions when winds upwind of the AP are sufficiently strong, downslope föhn winds can cause rapid warming over the lee slopes of the mountains and LCIS, temporarily disrupting the climatological west-east temperature gradient.

2.2. Atmospheric Model

We use archived data from the Antarctic Mesoscale Prediction System (AMPS, (Powers et al., 2012)). AMPS is a numerical weather prediction (NWP) system for the Antarctic region, run operationally by the Mesoscale and Microscale Meteorology Division of the National Center for Atmospheric Research. A brief summary of the model configuration is given here, but the reader is referred to the more complete description given by King et al. (2015) and in the references given below.

AMPS is implemented using the Weather Research and Forecasting (WRF) atmospheric model and, in the 2010–2011 melt season, used the nonhydrostatic WRF v3.0.1 with modifications to improve the representation of the surface energy balance over permanently ice-covered regions (Hines & Bromwich, 2008). The

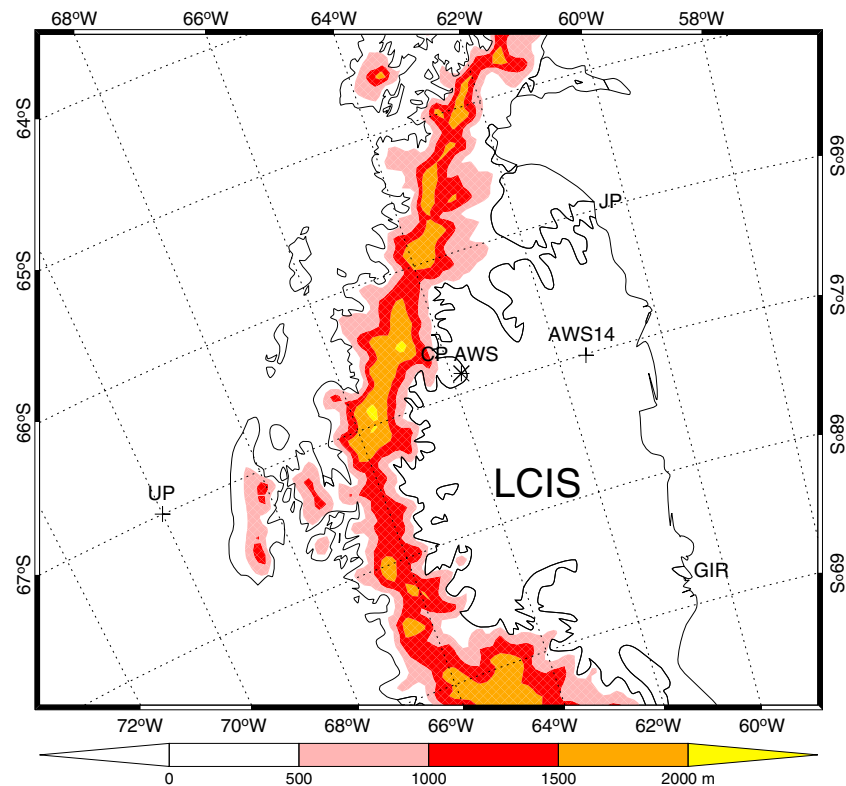


Figure 1. A map of the study area, showing Larsen C Ice Shelf (LCIS) between the Jason Peninsula (JP) and Gipps Ice Rise (GIR). Also shown are the locations of automatic weather stations AWS14 and CP AWS, and the upwind reference point, UP. Color shading shows the AMPS model orography.

model was run on a series of nested domains, the outermost of which covered Antarctica and much of the Southern Ocean at 45 km horizontal resolution. A nested 15 km resolution domain covered the Antarctic continent and, within this, a 5 km resolution domain covered the AP region.

Lateral boundary conditions for the outer (45 km) domain were taken from the Global Forecast System (GFS) 0.5° global NWP system run by the U.S. National Centers for Environmental Prediction and were updated every 6 h. Two runs of the AMPS system were carried out every day, starting from GFS analyses (together with regional data assimilation within the AMPS domain) at 0000 UTC and 1200 UTC. Forecasts on the 5 km AP grid were run to $T + 36$ h for each of these initializations. Previous investigations of flow over complex orography in Antarctica using data from AMPS indicate that the atmosphere in the 5 km model is fully adjusted to the high-resolution topography and land surface by the $T + 12$ forecast (Seefeldt & Cassano, 2008; Steinhoff et al., 2009). We have therefore chosen to use model output from the $T + 12$ and $T + 18$ forecasts from both model initialization times. Taken together, these provide us with a continuous 6-hourly series of model output fields. It is important to recognize that AMPS has not been optimized as a research tool as its primary purpose is the provision of timely forecasts to support U.S. Antarctic Program operations. However, the archive of high-resolution AMPS forecasts that extends back to 2006 provides a valuable resource for Antarctic climate studies. In this study, while recognizing the limitations of the model, we exploit the archive to move beyond case studies (e.g., Elvidge et al., 2015, 2016; Grosvenor et al., 2014) and hence develop a more climatological understanding of the impact of föhn on LCIS.

Grosvenor et al. (2014) demonstrated that the WRF model, run in a similar configuration to that used in AMPS, was able to produce a realistic simulation of a föhn wind event on the eastern side of the AP and LCIS when validated against instrumented aircraft observations. However, AMPS does have some weaknesses. King et al. (2015) validated AMPS simulations of the surface energy balance (SEB) against measurements at an automatic weather station (AWS) on LCIS. While AMPS simulated the turbulent fluxes of sensible and latent

heat quite well, modeled values of the radiative fluxes (which are the largest components of the SEB) were significantly biased when compared with observations. Similar biases were found by Bromwich et al. (2013) in an Antarctic-wide validation of the WRF model. AMPS also overestimated the occurrence of melting conditions at the AWS location. Given these biases, care needs to be taken when interpreting AMPS output. In this study, we concentrate on modeled differences between föhn and nonföhn conditions rather than absolute values.

2.3. Automatic Weather Station Data

For model validation we use observations from two automatic weather stations, the locations of which are marked in Figure 1. AWS14 (67°01'S, 61°30'W, 40 m above sea level (asl)) is situated toward the eastern edge of LCIS, and in addition to standard near-surface meteorological variables (pressure, temperature, relative humidity, and winds), it also measures downwelling and upwelling long- and shortwave tilt-corrected radiative fluxes. Data from AWS14 have been used to drive a snowpack model and hence produce an internally consistent set of surface energy balance components and snow surface temperature for this location (Kuipers Munneke et al., 2012). The second AWS was installed on 21 January 2011 at 66°52'S, 63°49'W, elevation 427 m asl, on the Cole Peninsula (henceforth CP), a low promontory extending eastward from the foot of the AP mountains. Only standard near-surface meteorological variables were measured by this AWS.

2.4. Surface Melt Observations From Remote Sensing

We use data from the Advanced Synthetic Aperture Radar (ASAR) carried by the European Space Agency's Envisat satellite to map the occurrence of surface melt over LCIS using the methodology described by Luckman et al. (2014). Briefly, the technique exploits the strong contrast in C-band microwave backscatter between liquid water and dry snow or ice to detect the occurrence of melt. A drop in backscatter beyond a threshold from the winter mean value indicates melt in the snowpack. ASAR images are available on average every 2 days and have a high spatial resolution of around 150 m.

2.5. Calculating Surface Energy Balance and Melt From AMPS Data

The energy budget at the surface of a snowpack can be written as

$$SW_{\downarrow} + SW_{\uparrow} + LW_{\downarrow} + LW_{\uparrow} + H_S + H_L = E \quad (1)$$

where SW_{\downarrow} and SW_{\uparrow} are, respectively, the downwelling and upwelling components of shortwave radiation, LW_{\downarrow} and LW_{\uparrow} are the downwelling and upwelling components of longwave radiation, H_S and H_L are, respectively, the turbulent fluxes of sensible and latent heat. The residual of these fluxes, E , is the net energy flux available for heating, cooling, or melting the snowpack. We use the sign convention that energy fluxes directed toward the snow surface are positive, so a positive value of E means that the surface layers of the snowpack are warming and/or melting. We assume that if the snow surface is at melting point and E is positive (i.e., directed downward, toward the snow surface), all of E is available to melt the snowpack and hence define the surface melt energy flux E_{melt} as

$$E_{\text{melt}} = \begin{cases} 0 & T_s < 0^{\circ}\text{C} \\ \max(0, E) & T_s = 0^{\circ}\text{C} \end{cases} \quad (2)$$

where T_s is the snow surface temperature.

All of the variables on the left-hand side of (1) are available in the AMPS 6-hourly output.

2.6. Identifying Föhn Conditions Using AMPS Data

Föhn is, by definition, a near-surface phenomenon, and the occurrence of föhn events is often detected by identifying the rapid changes in near-surface temperature, humidity, and wind speed that are associated with the onset and cessation of such events, for example, Cape et al. (2015). In this study we take a different approach and, instead, use atmospheric model data to identify the broad-scale flow patterns associated with föhn winds. We argue that as our approach is not reliant on near-surface data from a single location, it should give a better indication of the occurrence of föhn over a wider area. Furthermore, it is not reliant on the model's ability to simulate accurately the rapid changes in surface variables associated with the onset and cessation of föhn.

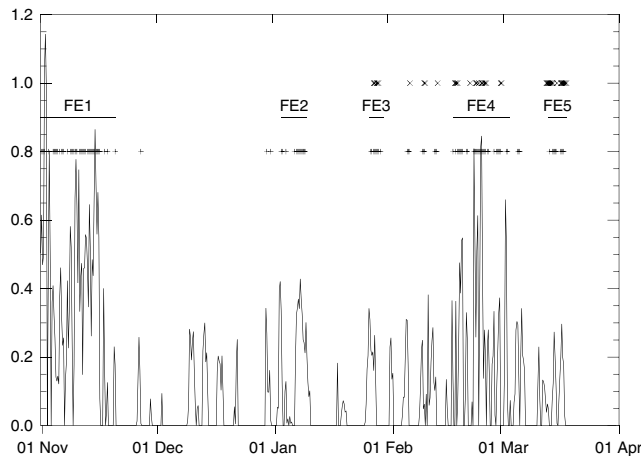


Figure 2. Occurrence of föhn during November 2010 to March 2011. Plus signs indicate times when föhn conditions were detected in 6-hourly AMPS fields using the criterion described in section 2.6 and crosses show when the relative humidity at CP AWS (from 21 January 2011) was below 60% (see supporting information). FE1–5 indicate the five föhn episodes defined in Table 1. Also shown (solid line) is a time series of the Froude number of flow upwind of the Antarctic Peninsula (see section 3.2).

Elvidge et al. (2016) and Orr et al. (2008) have shown that the occurrence and structure of föhn winds to the east of the AP mountains depends on the upwind flow, which can be characterized by the Froude number, Fr , a nondimensional parameter defined by

$$Fr = U/NH \tag{3}$$

where H is the height of the mountain barrier, and U and N are, respectively, the component of wind perpendicular to the mountain barrier and the Brunt-Vaisala frequency, both characteristic of the undisturbed flow upstream of the barrier. In the case of small Fr , the upstream flow is predominantly blocked; that is, only the uppermost portion of the upwind flow is able to pass over the barrier. Warming adiabatically as it descends, this air forms a warm, dry föhn wind over the lee slopes, which may extend onto LCIS. As Fr increases, air from progressively lower levels upstream is able to flow over the barrier and there is a transition at some critical Froude number, Fr_c , from a “nonlinear” (or partially blocked) to a “linear” (or “flow-over”) regime. The föhn’s characteristics lead to different warming mechanisms dominating in these two regimes (see Elvidge & Renfrew, 2016 for details).

While the two flow regimes give somewhat different patterns of föhn warming over LCIS (Elvidge et al., 2016), they are both characterized

by cross-barrier warming, with an increase in potential temperature between a given level upwind of the AP and the same level downwind of the mountains. We have, therefore, developed an algorithm to detect the occurrence of föhn based on west-east variations in potential temperature in the AMPS model. Our algorithm is as follows:

1. Determine the westerly component of the modeled wind, u_{up} , and modeled potential temperature, θ_{up} , at a location UP that is representative of conditions upwind (west) of the AP mountains, and at an elevation h_{up} that is just above the crest of the AP directly east of UP.
2. If $u_{up} \geq 2 \text{ m s}^{-1}$ (i.e., there is a clear flow from west to east across the AP mountains), calculate the elevation of the θ_{up} isentrope due eastward from UP over the AP mountains and LCIS.
3. Determine the minimum elevation, h_{min} , of the θ_{up} isentrope in the region to the east of the mountain crest and over LCIS.
4. If $\Delta h = h_{up} - h_{min}$ (i.e., the maximum lowering of the reference isentrope to the east of the mountains) exceeds some specified threshold, then *föhn conditions* are detected. We define a *föhn day* as a calendar day on which föhn conditions were detected in at least one of the four model forecast fields (0000, 0600, 1200, and 1800 UTC) for that day.

In what follows, we use 67°S, 70°W as our upwind reference location, UP. This point is approximately 150 km upwind of the AP mountains and should be representative of the undisturbed upwind flow (Orr et al., 2008). We set $h_{up} = 2,000 \text{ m}$ (i.e., just above the mountain crest at this latitude) as our upwind reference elevation. We have chosen $\Delta h \geq 500 \text{ m}$ as the criterion for defining the occurrence of föhn conditions. Our justification of this choice is given in supporting information S1.

3. Results

3.1. Occurrence of Föhn During the 2010–2011 Melt Season

Figure 2 shows the times when föhn conditions (as defined in section 2.6) were detected between 1 November 2010 and 31 March 2011. Out of a total of 604 6-hourly model fields, 127 (21%) meet our definition of föhn conditions over this period. Using the definitions in section 2.6, this gives 54 föhn days (36%) out of a total of 151 days in the melt season. Using a more stringent definition, $\Delta h \geq 1,000 \text{ m}$, reduces the number of föhn days to 34, while using $\Delta h \geq 200 \text{ m}$ increases the number of föhn days slightly to 59. The frequency with which föhn is detected also depends on the chosen latitude for the potential temperature transect. Moving the latitude of the transect from 67°S to 68°S (an appropriate latitude for defining the occurrence of föhn over the southern part of LCIS) and reducing h_{up} to 1,700 m to reflect the lower height of the mountain barrier at

Table 1
Upwind Flow Variables During Föhn and Nonföhn Conditions Determined From AMPS 6 h Fields

Subset	Start date	End date	No. of fields	\bar{Fr}	\bar{U} (m s ⁻¹)
All	1 Nov 2010	31 Mar 2011	604	0.11	-1.33
FE1	1 Nov 2010	20 Nov 2010	80	0.36	7.64
FE2	3 Jan 2011	9 Jan 2011	28	0.17	3.56
FE3	26 Jan 2011	29 Jan 2011	16	0.12	0.31
FE4	17 Feb 2011	3 Mar 2011	60	0.22	3.17
FE5	14 Mar 2011	18 Mar 2011	20	0.10	1.42
All föhn			127	0.31	7.73
All nonföhn			477	0.06	-3.75

Note. "All" refers to all fields during the study period, "All föhn" to only those fields classed as föhn conditions using the criterion of section 2.6 and "All nonföhn" to all fields that do not meet this criterion. FE1–5 are the five föhn episodes defined in section 3.1.

this latitude reduces the number of föhn days identified to 46. Cape et al. (2015) also found that the frequency of occurrence of föhn reduced from north to south along the eastern side of the AP. This probably reflects the north-south gradient in the strength of the climatological westerly winds in this region (Marshall et al., 2006).

The occurrence of föhn is not evenly distributed through the season but is clustered into episodes of persistent föhn conditions. Defining a *föhn episode* as a period of at least three *föhn days*, with no more than one consecutive nonföhn day intervening, identifies five föhn episodes (FEs) during the 2010–2011 melt season, ranging from 4 to 20 days duration (Table 1). FE3 corresponds roughly with the "case B" föhn event studied by Elvidge et al. (2015), while their "case C" occurred during FE1. Their "case A" was too short to meet our definition of a föhn episode although, as seen in Figures 2 and S2, our technique does detect transient föhn conditions over this period.

The uneven distribution of föhn through the melt season presents problems when contrasting surface energy balance during föhn and nonföhn conditions as some of the energy fluxes that contribute to the surface energy balance (notably the downwelling shortwave radiation) exhibit a strong seasonal cycle. Hence, the difference in surface energy fluxes between föhn and nonföhn conditions will reflect not only the impact of föhn but also the temporal distribution of föhn events through the season. Ideally, this ambiguity would be avoided by removing the mean seasonal cycle from all variables before carrying out the analysis. Unfortunately, changes to the AMPS radiation scheme over time mean that we do not have a sufficient number of annual cycles with a stable model configuration to enable us to determine a mean seasonal cycle accurately. Consequently, here we note where the seasonal cycle may lead to biases and put emphasis on the spatial pattern of the differences between föhn and nonföhn conditions, which is less subject to bias than the absolute values.

3.2. Upwind Meteorological Conditions Associated With Föhn

The five föhn episodes (FEs) correspond well with periods of strengthened westerly winds to the west of the AP, as illustrated by elevated Froude numbers in Figure 2. Following Elvidge et al. (2015), we have calculated Fr at location UP from equation (3) by setting U to the average westerly wind component from model levels between 200 and 2,000 m elevation and calculating N from the model potential temperature difference between 200 and 2,000 m. We use $H = 2,000$ m for the mountain barrier height and set Fr to zero if $U < 0$ (i.e., easterly flow). Note that Fr is simply the reciprocal of the nondimensional mountain height parameter, \hat{h} , used by Elvidge et al. (2015). Mean values of Fr during föhn and nonföhn conditions are shown in Table 1. Föhn conditions detected using our criterion mostly occur for Fr values greater than about 0.2, while Fr rarely exceeded 1 during the season studied. Nonrotating hydraulic theory predicts $Fr_c = O(1)$ and would thus indicate a partially blocked, nonlinear flow regime under such conditions. However, Orr et al. (2008) have shown that Coriolis effects significantly reduce Fr_c for a high-latitude barrier such as the AP so the regime $0.2 \leq Fr \leq 1.0$ will include both nonlinear and linear flows. Note that variations in U are much greater than those in N , and $Fr = 0.2$ corresponds approximately to $U \approx 5$ m s⁻¹.

3.3. The Impact of Föhn on Surface Meteorology and Surface Energy Balance

In order to investigate the impact of föhn on surface conditions over LCIS, we have calculated *föhn composite anomalies* (i.e., means of a variable for all föhn days minus its mean value over the whole of the 2010–2011 melt season) for key meteorological and surface energy balance variables. Figure 3 shows maps of föhn composite anomalies for near-surface meteorological variables over the AP mountains and LCIS. The leeside warming associated with föhn conditions is clearly visible in the 2 m air temperature (T_a) anomaly, with the greatest warming (>3 K) seen over the lowermost part of the eastern slopes of the AP mountains. This warming extends eastward onto LCIS but decreases rapidly moving away from the foot of the mountains. Surface temperatures (T_s) show a similar response to föhn although the anomalies are smaller. Warming of 1–2 K is seen across the mountains, but anomalies across LCIS are mostly less than 1 K, except in the very northern part of the ice shelf. During föhn, near-surface relative humidity with respect to ice (RH_i) over the

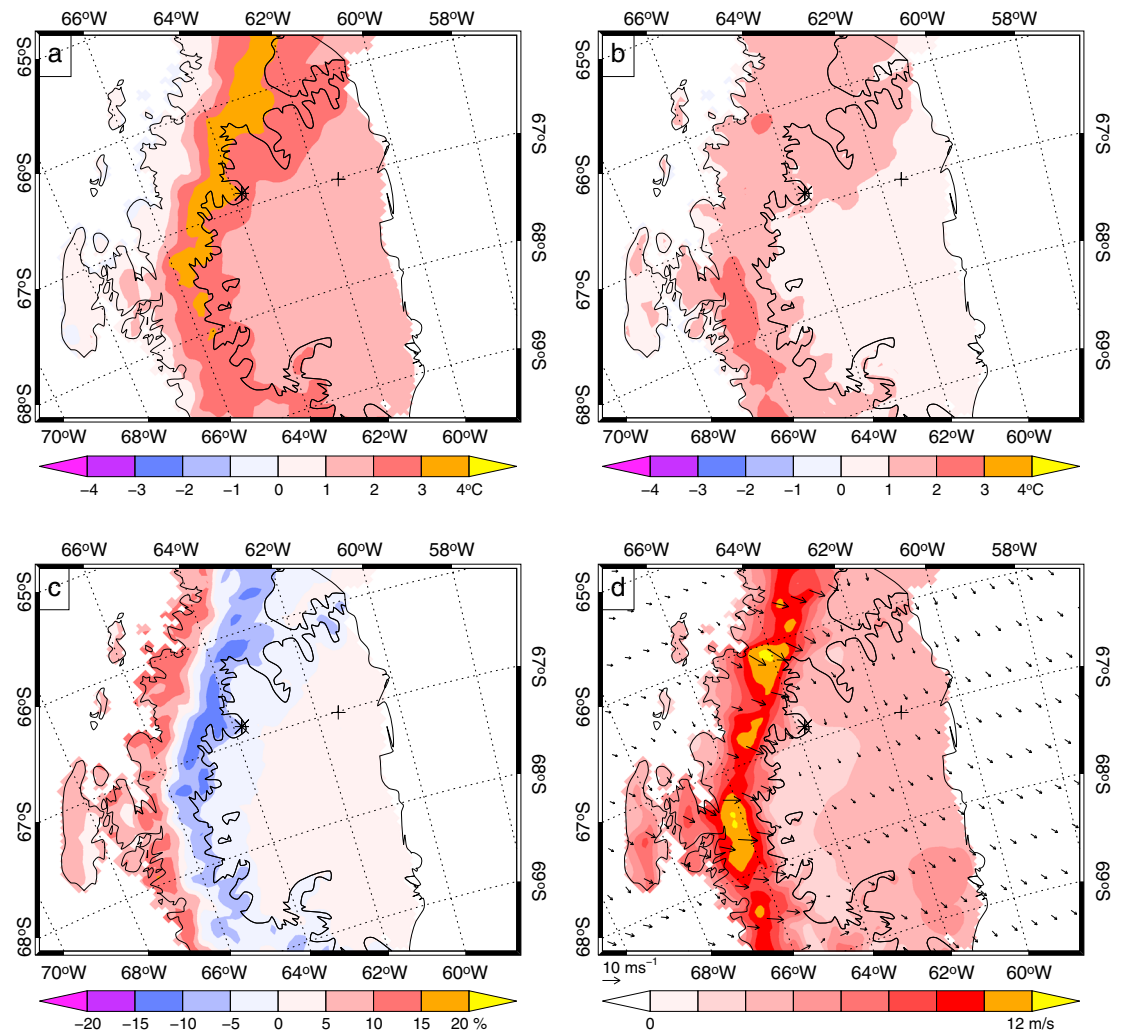


Figure 3. Föhn composite anomalies for (a) 2 m air temperature, (b) surface temperature, (c) relative humidity, and (d) 10 m wind speed (contour interval 1.5 m s^{-1}) and wind vector. In this and subsequent figures model sea points have been masked out and the locations of AWS 14 (plus sign) and CP AWS (asterisk) have been marked.

eastern slopes of the AP mountains is reduced by up to 15%, but little change is seen over much of LCIS. The 10 m wind anomalies indicate significantly stronger westerly to northwesterly flow over the crest of the AP and over the eastern slopes of the mountains during föhn conditions, with smaller and largely northerly wind anomalies over LCIS itself. The 10 m wind speed (U_{10}) anomalies show little sign of the “föhn jets”—narrow jets emanating from the inlets at the foot of the mountains during föhn conditions—that are a feature of the aircraft observations and 1.5 km grid resolution simulations carried out by Elvidge et al. (2015). There are two possible reasons for this. First, the alignment of the jets varies with the direction of the upwind flow, so the distinct character of the jets may be lost when averaging over many föhn events. Second, Elvidge et al. (2015) showed that the jets were much weaker in simulations at 4 km resolution (i.e., comparable to AMPS) than at 1.5 km resolution.

The pattern of anomalies seen in Figure 3 is broadly consistent with the expected signature of a warm, dry westerly föhn wind descending the lee slopes of the AP mountains and reaching the westernmost part of LCIS. Concurrent with the anomalies in basic meteorological variables, we also see a clear signature of föhn in the anomalies of surface energy balance variables (Figure 4). During föhn conditions, the turbulent flux of sensible heat exhibits large negative anomalies on the upwind slopes of the AP mountains and even larger ($>40 \text{ W m}^{-2}$) positive anomalies to the east of the AP crest, with smaller positive anomalies extending eastward across LCIS. However, these positive anomalies are largely balanced by corresponding negative

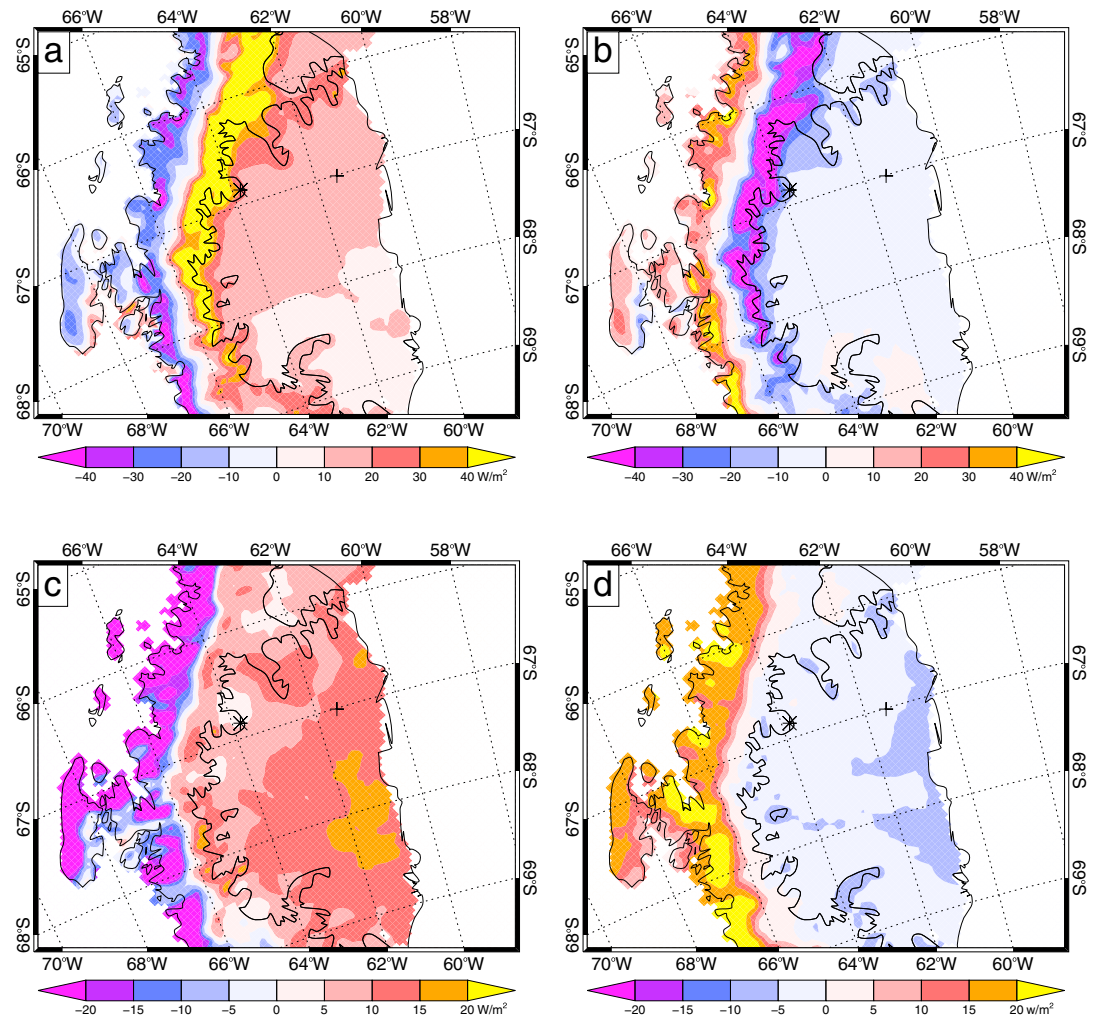


Figure 4. Föhn composite anomalies for (a) sensible heat flux, (b) latent heat flux, (c) downwelling shortwave radiation (calculated indirectly using the shortwave transmissivity anomaly—see text for details), and (d) downwelling longwave radiation.

anomalies in the turbulent flux of latent heat. Under föhn conditions, air ascends the western slopes of the AP mountains and cools adiabatically, generating an upward (negative) sensible heat flux. On the eastern slopes of the mountains, the warm, dry descending föhn wind generates a large downward (positive) sensible heat flux and upward (negative) latent heat flux. The increased wind speeds seen on the eastern slopes during föhn conditions (Figure 3d) generate enhanced turbulent mixing on this side of the mountains and contribute to the large flux anomalies seen here.

Föhn also impacts on the radiative fluxes of energy at the surface. During the 2010–2011 melt season, most föhn days occurred toward the beginning or the end of the season, with most nonföhn days clustered around the summer solstice when downwelling shortwave radiation is (climatologically) at its highest. As a result, föhn composite anomalies for downwelling shortwave radiation are strongly biased by the seasonal cycle and do not give a useful indication of the impact of föhn on radiative fluxes. To avoid this bias, we have calculated the shortwave atmospheric transmissivity

$$\tau_{SW} = SW_{\downarrow} / SW_{\downarrow}^{TOA} \tag{4}$$

where SW_{\downarrow}^{TOA} is the incident shortwave radiation at the top of the atmosphere. We have then calculated föhn composite anomalies of τ_{SW} and, in Figure 4c, we show the composite anomaly field of τ_{SW} multiplied by the seasonal mean of SW_{\downarrow}^{TOA} . This provides a less biased indication of the impact of föhn on SW_{\downarrow} than the

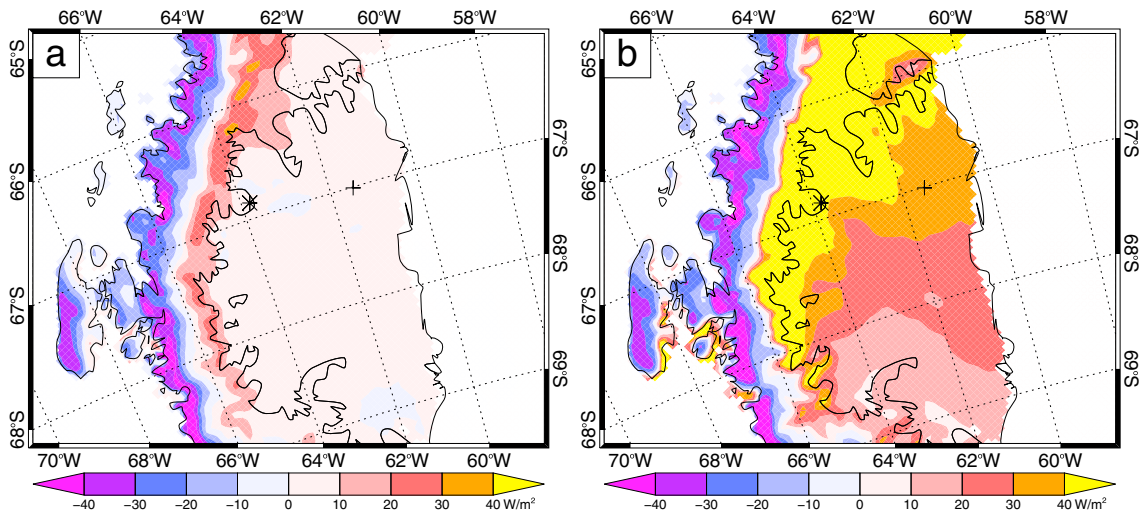


Figure 5. Composite anomalies for sensible heat flux for two different ranges of upstream Froude number, Fr : (a) $0.2 < Fr \leq 0.4$ (nonlinear föhn, 204 model fields) and (b) $Fr > 0.4$ (linear föhn, 96 model fields).

straightforward composite anomaly. Figure 4c reveals a distinct spatial pattern, with negative anomalies in $SW\downarrow$ over the western slopes of the mountains, and positive anomalies to the west of the AP and over LCIS. During föhn conditions, ascending air to the west of the AP will be associated with increased cloud cover which will reduce $SW\downarrow$ (relative to that observed under nonföhn conditions at the same time of year); while, to the east of the mountains and over LCIS, descending air will be associated with reduced cloud cover and enhanced $SW\downarrow$ (again relative to nonföhn conditions). The seasonal cycle in $LW\downarrow$ is weaker than that in $SW\downarrow$ so composite anomalies are not strongly biased by the seasonal cycle. The spatial pattern of the composite anomaly for $LW\downarrow$ (Figure 4d) is the inverse of that for $SW\downarrow$. Increased cloud cover west of the AP during föhn leads to enhanced $LW\downarrow$, while reduced cloud cover to the east results in reduced $LW\downarrow$.

Figures 3 and 4 clearly illustrate the impact of föhn on near-surface conditions averaged over the melt season. However, there is considerable variation in this impact between individual föhn events. Elvidge et al. (2016) examined the signatures of three föhn events over LCIS and showed that both the magnitude and the spatial extent of föhn warming depended on the nature of the flow during the föhn event. Nonlinear (low Fr) flows were associated with a small warming, largely confined to the extreme west of LCIS, while linear (high Fr) flows were associated with a much larger area of warming that extended eastward across LCIS. Figure 5

shows composite anomalies of H_5 for two ranges of Fr : $0.2 < Fr \leq 0.4$ (a nonlinear composite, Figure 5a) and $Fr > 0.4$ (a linear composite, Figure 5b). While both composites show some resemblance to the corresponding föhn composite anomaly (Figure 4a), it is clear that the more linear flows included in the composite shown in Figure 5b have a greater impact over a wider area than do the more nonlinear flows included in Figure 5a.

We have used measurements from AWS14 and CP AWS to carry out a limited validation of the model results. Modeled and observed föhn composite anomalies of meteorological and SEB variables at AWS14 are shown in Table 2. Both model and observations indicate warming of similar magnitude during föhn. The anomalies in sensible and latent heat fluxes are of opposite sign in both model and observations, and the magnitude of the modeled anomalies is in reasonable agreement with those observed. A 3% increase in shortwave transmissivity during föhn conditions is seen in both model and observations, despite the significant positive bias in modeled mean $SW\downarrow$ compared to observations (King et al., 2015). Modeled anomalies in relative humidity and

Table 2

Seasonal Means and Föhn Composite Anomalies ($\Delta_{föhn}$) for Observed and Modeled Meteorological and SEB Variables at AWS14

Variable	Observations		Model	
	Mean	$\Delta_{föhn}$	Mean	$\Delta_{föhn}$
T_a (°C)	-5.69	+1.78**	-5.15	+1.52**
T_s (°C)	-5.91	+1.24**	-5.04	+0.88*
RH_i (%)	91.3	-3.40**	96.8	+0.16
U_{10} ($m\ s^{-1}$)	4.66	-0.42*	5.09	+0.61*
H_s ($W\ m^{-2}$)	-2.74	+6.40**	-1.85	+13.2**
H_l ($W\ m^{-2}$)	-8.55	-0.11	-6.59	-4.3**
$SW\downarrow$ ($W\ m^{-2}$)	238.5	+0.33	284.2	-5.7
$LW\downarrow$ ($W\ m^{-2}$)	267.5	-8.52**	261.3	-3.3
τ_{sw}	0.61	+0.03	0.76	+0.03
E_{melt} ($W\ m^{-2}$)	8.84	+4.23**	12.9	+0.6

*Anomaly significant at $p = 0.05$ or better. **Anomaly significant at $p = 0.01$ or better.

Table 3
Means and Föhn Composite Anomalies ($\Delta_{\text{föhn}}$) for Observed and Modeled Meteorological Variables at CP AWS for the Period 22 January to 31 March 2011

Variable	Observations		Model	
	Mean	$\Delta_{\text{föhn}}$	Mean	$\Delta_{\text{föhn}}$
T_a (°C)	-6.91	+5.40**	-6.99	+4.12**
RH_i (%)	78.0	-8.23**	93.9	-7.50**
U_{10} (m s ⁻¹)	4.91	-1.37	5.92	+0.15

**Anomaly significant at $p = 0.01$ or better.

wind speed are of opposite sign to those observed, but the absolute values of both modeled and observed anomalies are small at this location. CP AWS was not installed until 21 January, so föhn composite anomalies of meteorological variables have been calculated for the period 22 January to 31 March (Table 3). Because the AMPS model topography in the vicinity of CP AWS differs slightly from the real topography, model data have been extracted from a point close to the location of CP AWS where the model topography has the same elevation as the actual AWS site. As expected from Figure 3, the impact of föhn at this location, situated close to the AP mountains, is greater than that seen at AWS14. Model data and observations both indicate significant

near-surface warming and drying during föhn, with good agreement on the magnitudes of the changes. Neither the model nor the AWS indicate significant changes in wind speed. While Figure 3d indicates that wind speeds over the eastern slopes of the AP mountains generally increase during föhn conditions, the local topography around CP AWS is complex. The AWS is not located in one of the regions where Elvidge et al. (2015) identified “föhn jets,” where wind speed is particularly sensitive to the presence of föhn.

Overall, Tables 3 and 4 confirm that AMPS shows some skill in simulating the impact of föhn on near-surface meteorology and surface energy fluxes. However, the modeled response of melt to föhn appears to be somewhat weaker than that seen in observations. The difference in response reflects both mean biases in elements of the modeled climate and the model’s inability to simulate the impact of föhn on some energy fluxes realistically.

In summary, the occurrence of föhn causes large changes in individual components of the modeled surface energy balance across the study area and these agree reasonably well with the limited validation data that are available. The spatial patterns of the föhn composite anomalies are (at least qualitatively) consistent with the conceptual model of a warm, dry föhn wind descending the eastern slopes of the AP mountains and flowing eastward across LCIS, with the extent of eastward propagation depending strongly on upstream flow conditions.

3.4. The Impact of Föhn on Surface Melt

Figure 6 shows föhn composite anomalies for the net surface energy flux, E , and the melt energy flux, E_{melt} . While composite anomalies in individual components of the SEB can exceed 50 W m^{-2} , anomalies in E and E_{melt} are an order of magnitude smaller, as positive anomalies in H_s and $SW\downarrow$ during föhn are largely balanced by compensating anomalies of similar magnitudes but of opposite signs in H_L and $LW\downarrow$. While our limited validation data (Table 2) show some observational evidence for this compensation, there are differences between the modeled and observed response to föhn. Since the change in E is the sum of the large, and partially compensating, changes in the individual fluxes, any small errors in the modeled fluxes or their response

to föhn will have a large impact on how modeled E responds to föhn. A further possible reason for the apparent insensitivity of melt energy to föhn is bias due to the uneven distribution of föhn conditions through the season, as discussed in section 3.1. During 2010–2011, föhn mostly occurred early or late in the season, when $SW\downarrow$, a major component of E , was relatively small. As a result, the seasonal means of E and E_{melt} during föhn are lower than they would be if föhn conditions had been evenly distributed through the season. We therefore note that the actual response of melt to föhn may be greater than that suggested by the AMPS model results shown in Figure 6.

As well as affecting the intensity of melt through its impact on the SEB, föhn can affect the frequency or duration of melt through its impact on surface temperature. We quantify this latter impact by examining the melt fraction; that is, the fraction of days during a particular period when modeled surface temperatures reached 0°C in at least one of the 6-hourly model fields for that day.

Table 4
Means of Modeled and Observed Meteorological and SEB Variables at AWS14 Over 10–18 November (Föhn) and 19–25 November 2010 (Nonföhn)

Variable	10–18 Nov		19–25 Nov		$\Delta_{\text{föhn}}$	
	AMPS	AWS	AMPS	AWS	AMPS	AWS
T_a (°C)	-1.0	-0.4	-3.2	-5.6	+2.2	+5.2
RH_i (%)	91	79	95	92	-4	-13
U_{10} (m s ⁻¹)	8.6	6.0	5.2	5.6	+3.4	+0.4
H_s (W m ⁻²)	31.5	16.5	-9.1	-6.8	+40.6	+23.3
H_L (W m ⁻²)	-25.1	-13.0	-5.9	-11.1	-19.2	-1.9
SW_{net}	66.6	63.1	60.3	37.8	+6.3	+25.3
LW_{net}	-33.5	-49.9	-11.7	-25.0	-21.9	-24.9
E (W m ⁻²)	39.5	16.7	33.7	-5.1	+5.8	+21.8
E_{melt} (W m ⁻²)	30.3	29.6	21.7	0.9	+8.6	+28.7

Note. $\Delta_{\text{föhn}}$ is the value for the föhn period minus that for the nonföhn period. AWS14 values are from Kuipers Munneke et al. (2012), Table 3.

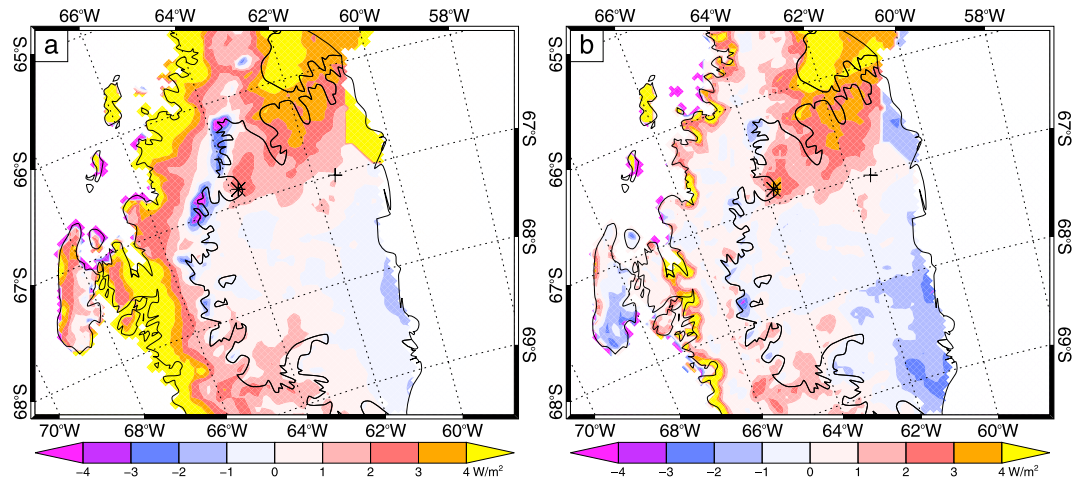


Figure 6. Föhn composite anomalies for (a) net surface energy flux, E , and (b) melt energy flux, E_{melt} .

Figures 7a and 7b show modeled melt fraction for November and December 2010, respectively. While an extended föhn episode (FE1, 1–20 November) occurred during November 2010, in contrast, December was characterized by an almost complete absence of föhn conditions (see Figure 2). In the AMPS simulations, there is a clear contrast between the 2 months, with higher melt fractions modeled across LCIS north of

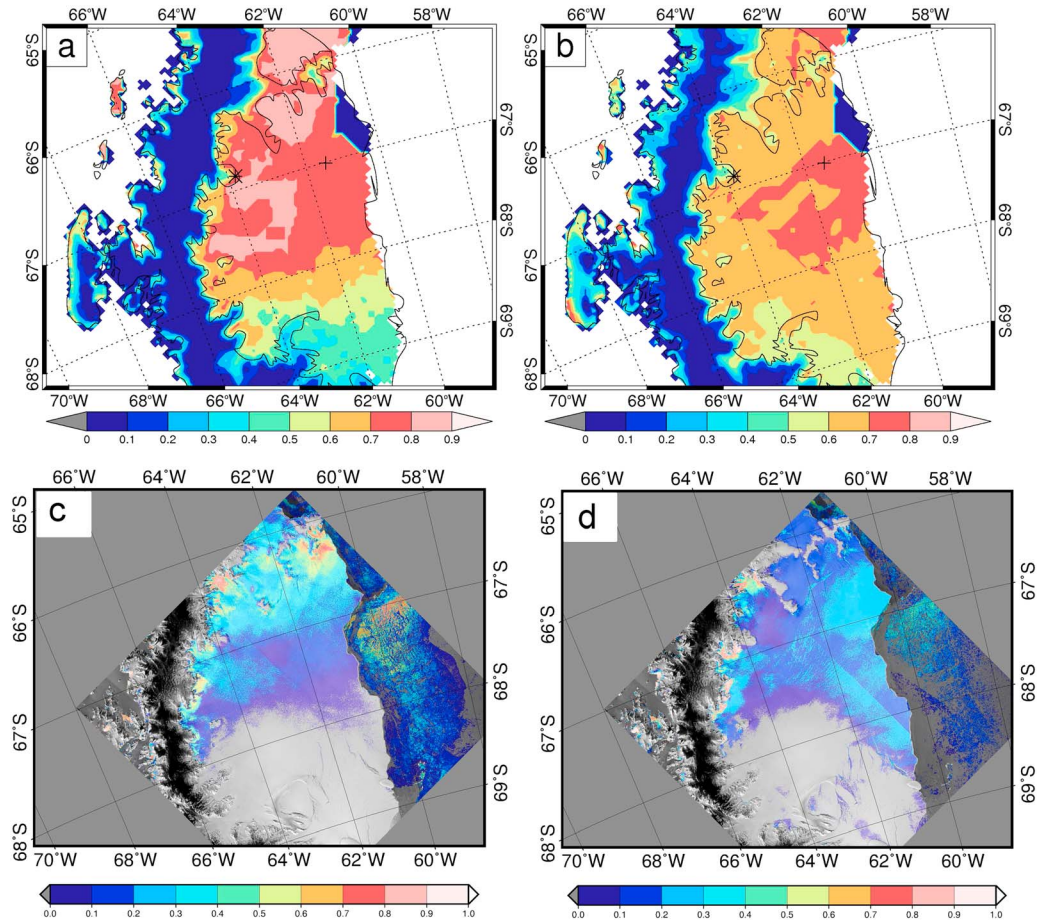


Figure 7. Melt fraction from AMPS simulations for (a) November and (b) December 2010, together with corresponding melt fractions calculated from (c and d) Envisat radar backscatter data. In Figures 7a and 7b, AMPS sea points have been masked white. In Figures 7c and 7d, areas for which processed Envisat data are not available are masked dark gray.

68°S during November than during December. Persistent föhn conditions during November thus appear to have promoted enhanced surface melt across a wide area of LCIS. By contrast, generally nonföhn conditions during December were associated with reduced occurrence of melt, despite downwelling shortwave radiation being higher in December as the summer solstice is approached.

Figures 7c and 7d show the corresponding observed (Envisat) melt fractions. Across most of LCIS, modeled melt fraction exceeds that observed by up to a factor of 2. This overprediction of the occurrence of melt by AMPS was also noted by King et al. (2015), who attributed it to excessive surface heating associated with the positive bias in modeled SW_{\downarrow} . Despite this mean bias, the spatial and temporal variability of melt in the model shows some similarity with that observed. Both model and observations show a higher melt fraction across the northern part of LCIS in November (persistent föhn conditions) than during December (föhn almost entirely absent). However, the observations reveal fine-scale spatial structure that is not present in the AMPS average melt fraction. In particular, the observations show strong and persistent melt occurring in the inlets along the foot of the AP mountains at the western edge of LCIS during both November and December. Although the AMPS simulations do indicate that föhn has its greatest impact on temperature and individual energy fluxes at the foot of the mountains, the largest melt fractions simulated by AMPS are displaced to the east over LCIS. Furthermore, the persistence of melt in the inlets through December (from Envisat observations), when föhn was almost entirely absent, suggests that föhn may not be the only process that controls melt in these locations.

4. Discussion and Conclusions

Data from the AMPS model have been used to investigate the impact of föhn on SEB and melt over LCIS and adjoining parts of the AP. Large changes occur in individual modeled components of the SEB during föhn conditions. However, increases (relative to the seasonal average) in downwelling shortwave radiation and sensible heat flux during föhn episodes are largely compensated for by corresponding decreases in downwelling longwave radiation and latent heat flux, so the modeled change in net energy flux is small.

Although föhn appears to have limited impact on modeled melt when averaged over the season studied, it is clear from both model and observational data that individual föhn episodes can have a significant impact on melt. The impact of FE1 on melt across a wide area of LCIS is clearly seen in the contrasting patterns of melt during November and December 2010. Both the AMPS model and Envisat observations show that föhn associated with this episode of strong, linear flow-over conditions caused enhanced melt across much of the northern part of LCIS during November, with lower melt rates seen in both model and observations during December, when föhn was largely absent. Model fields and measurements made at AWS14 (Kuipers Munneke et al., 2012) show that FE1 had a strong impact on surface melt right across LCIS. Table 4 contrasts modeled and observed SEB at AWS14 during two periods studied by Kuipers Munneke et al. (2012): 10–18 November 2010 (i.e., the end of FE1) and 19–25 November 2010 (mostly nonföhn conditions). The observations indicate that E_{melt} was almost 30 W m^{-2} greater during the föhn period while the model shows less than 10 W m^{-2} difference. Both model and observations show the net turbulent heat flux, $H_S + H_L$, increasing by about 20 W m^{-2} during föhn, although the partitioning of this change between sensible and latent heat flux differs considerably between AMPS and the AWS measurements. The modeled decrease in net longwave radiation during the föhn period agrees well with that observed, but the model shows a much smaller increase in net shortwave radiation during föhn than the observations. The failure of the model to capture the observed changes in shortwave radiation is almost certainly associated with the weaknesses in the model's representation of cloud microphysics that were noted by King et al. (2015).

Figure 2 and Table 1 show that FE1 was associated with high values of upstream Froude number as a result of the strong northwesterly winds that prevailed through much of November. Figure 5 and the cases studied by Elvidge et al. (2016) show that during such linear flow-over episodes, surface warming associated with the leeside föhn extends eastward from the foot of the AP mountains across much of LCIS while, during nonlinear episodes, warming is restricted to the immediate vicinity of the foot of the mountains. FE2, FE3, and FE5 are all associated with smaller values of Froude number than FE1 and can be categorized as nonlinear flows. During FE4, Froude numbers approach those seen during FE1 but little melt is either modeled or observed during this episode. While the middle of FE1 occurred approximately 41 days

before the summer solstice, the middle of FE4 is approximately 65 days after the solstice so SW_{\downarrow} is lower during this latter episode. The time of occurrence of FE4, together with somewhat weaker westerly winds than during FE1, thus explains why extensive melt is seen during FE1 but not during FE4.

While both model simulations and satellite observations indicate a connection between the occurrence of föhn and surface melt, there are some notable differences between the modeled and observed patterns. The Envisat observations show regions of high melt along the western margin of the ice shelf, particularly in the inlets where glaciers drain down into the ice shelf from the AP mountains. As noted in section 1, evidence for enhanced melt in this region has been provided by other techniques (Holland et al., 2011; Tedesco, 2009) so this feature is almost certainly genuine. The AMPS model does indicate a strong influence of föhn on near-surface air temperature and SEB components in this region but does not show enhanced melt here. The failure of the AMPS model to reproduce this feature may partly reflect the unrealistically weak response of modeled SEB to föhn that was discussed above.

The failure of the 5 km AMPS simulation to reproduce the föhn jets described by Elvidge et al. (2015) may contribute to the model's inability to simulate enhanced melt in the inlets during föhn. However, the observed persistence of melt in the inlets into December (when föhn was absent) suggests that the link between föhn and melt in this region may not be straightforward. One possibility is that strong and persistent melt in the inlets during FE1 lowered the albedo of this region through the development of melt ponds or metamorphosis of the snowpack. If these albedo anomalies persisted after the end of FE1 they could become self-sustaining through a positive feedback involving albedo and melt energy, particularly as SW_{\downarrow} increases through December. The AMPS model, which uses a fixed surface albedo, is unable to capture such feedbacks. A second possibility is that enhanced melt in the inlets is associated with meteorological phenomena other than föhn. Our identification of föhn through leeside lowering of an isentrope has meant that the focus of our study has been on "deep föhn" events, associated with westerly flow over the AP mountains. However, studies in the European Alps and elsewhere (e.g., Mayr et al., 2007) have shown that the pressure gradient associated with mountain-parallel winds can drive ageostrophic, föhn-like flows (known as "shallow föhn") through gaps in the mountain barrier. It is possible that such flows could be responsible for driving warming and melt in the inlets in the absence of strong, westerly cross-mountain flow. However, it is unlikely that such flows will be well resolved by the 5 km AMPS model.

While the focus of our study has been on the links between föhn occurrence, SEB and melt over short time periods during the 2010–2011 melt season, it is important to place this season within the context of the longer record. In order to do this, we have calculated a time series of the parameter Fr , as described in section 2.6 but using 6-hourly data from the European Centre for Medium-Range Weather Forecasts interim global reanalysis (ERA-interim) for 1979–2015. ERA-interim has a much lower horizontal resolution (~80 km) than AMPS. However, values of Fr calculated from ERA-interim agree very closely with those calculated from AMPS during the 2010–2011 melt season, indicating that ERA-interim provides a good simulation of conditions upwind of the AP. Following the results presented in section 3.2, we take $Fr \geq 0.2$ as an indicator of the occurrence of föhn. Using this indicator, the frequency of occurrence of föhn varies between 11% (2000–2001 melt season) and 40% (1992–1993 melt season) over the 37 melt seasons covered by the ERA-interim record. The 2010–2011 season (22%) ranks 28th in this series, making it typical of years with relatively weak westerly winds where blocked and partially blocked (nonlinear) flows prevail. The net impact of föhn on SEB and melt may be larger than that seen in our study during seasons when the westerlies are stronger.

We have demonstrated that the AMPS model can provide some insight into the processes that connect föhn and melt over LCIS. However, the utility of AMPS for these studies is limited by weaknesses in the model's representation of some components of the surface energy balance and their response to föhn. The weaknesses that we have identified in the AMPS operational forecasting model need to be addressed in order to develop research models that can accurately simulate melt over LCIS and the impact of föhn on melt in this region. Most importantly, the bias in modeled shortwave radiation identified by King et al. (2015) needs to be reduced and the seemingly unrealistic partitioning between sensible and latent heat flux under föhn conditions requires investigation. Additionally, there is a requirement to carry out model simulations at higher resolution. The AMPS 5 km simulations are unable to reproduce the region of high melt along the foot of the AP mountains that is a robust feature in several observational data sets. Case

studies carried out by Elvidge et al. (2015, 2016) have demonstrated that a model resolution of 1.5 km or better is required to simulate föhn flows, the associated föhn jets and the interaction with the boundary layer over LCIS accurately. It is thus likely that model simulations at higher resolution than 5 km will be required to understand the processes that drive melt in this topographically complex region.

Acknowledgments

The work reported in this paper was supported by the UK Natural Environment Research Council (NERC) under grants NE/G014124/1, NE/L006707/1, and NE/L005409/1. AWS14 is funded by the Netherlands Polar Program (NPP) of the Netherlands Organization of Scientific Research, Earth and Life Sciences section (NWO/ALW). We thank the Mesoscale and Microscale Meteorology Division of the National Center for Atmospheric Research for giving us access to the AMPS forecast archive, and Alan Gadian and Tony Phillips for assistance with accessing and processing the these data. AMPS model data are freely available through the Earth System Grid (www.earthsystemgrid.org). Data from AWS14 are available on request from IMAU, University of Utrecht (contact c.h. tijm-reijmer@uu.nl). CP AWS data may be obtained from the British Atmospheric Data Centre (Natural Environment Research Council, 2014).

References

- Abram, N. J., Mulvaney, R., & Arrowsmith, C. (2011). Environmental signals in a highly resolved ice core from James Ross Island, Antarctica. *Journal of Geophysical Research*, 116, D20116. <https://doi.org/10.1029/2011JD016147>
- Ashmore, D. W., Hubbard, B., Luckman, A., Kulesa, B., Bevan, S., Booth, A., ... Holland, P. R. (2017). Ice and firn heterogeneity within Larsen C Ice Shelf from borehole optical televiewing. *Journal of Geophysical Research: Earth Surface*, 122(5), 1139–1153. <https://doi.org/10.1002/2016JF004047>
- Barrand, N. E., Vaughan, D. G., Steiner, N., Tedesco, M., Kuipers Munneke, P., van den Broeke, M. R., & Hosking, J. S. (2013). Trends in Antarctic Peninsula surface melting conditions from observations and regional climate modeling. *Journal of Geophysical Research: Earth Surface*, 118(1), 315–330. <https://doi.org/10.1029/2012JF002559>
- Bromwich, D. H., Otieno, F. O., Hines, K. M., Manning, K. W., & Shilo, E. (2013). Comprehensive evaluation of polar weather research and forecasting model performance in the Antarctic. *Journal of Geophysical Research: Atmospheres*, 118(2), 274–292. <https://doi.org/10.1029/2012JD018139>
- Cape, M. R., Vernet, M., Skvarca, P., Marinsek, S., Scambos, T., & Domack, E. (2015). Foehn winds link climate-driven warming to ice shelf evolution in Antarctica. *Journal of Geophysical Research: Atmospheres*, 120(21), 11,037–11,057. <https://doi.org/10.1002/2015JD023465>
- Cook, A. J., & Vaughan, D. G. (2012). Overview of areal changes of the ice shelves on the Antarctic Peninsula over the past 50 years. *The Cryosphere*, 4(1), 77–98.
- Elvidge, A. D., & Renfrew, I. A. (2016). The causes of foehn warming in the lee of mountains. *Bulletin of the American Meteorological Society*, 97(3), 455–466. <https://doi.org/10.1175/BAMS-D-14-00194.1>
- Elvidge, A. D., Renfrew, I. A., King, J. C., Orr, A., & Lachlan-Cope, T. A. (2016). Foehn warming distributions in nonlinear and linear flow regimes: A focus on the Antarctic Peninsula. *Quarterly Journal of the Royal Meteorological Society*, 142(695), 618–631. <https://doi.org/10.1002/qj.2489>
- Elvidge, A. D., Renfrew, I. A., King, J. C., Orr, A., Lachlan-Cope, T. A., Weeks, M., & Gray, S. L. (2015). Foehn jets over the Larsen C Ice Shelf, Antarctica. *Quarterly Journal of the Royal Meteorological Society*, 141(688), 698–713. <https://doi.org/10.1002/qj.2382>
- Grosvenor, D. P., King, J. C., Choullarton, T. W., & Lachlan-Cope, T. (2014). Downslope föhn winds over the Antarctic Peninsula and their effect on the Larsen ice shelves. *Atmospheric Chemistry and Physics*, 14(18), 9481–9509. <https://doi.org/10.5194/acp-14-9481-2014>
- Harig, C., & Simons, F. J. (2015). Accelerated West Antarctic ice mass loss continues to outpace East Antarctic gains. *Earth and Planetary Science Letters*, 415, 134–141. <https://doi.org/10.1016/j.epsl.2015.01.029>
- Hines, K. M., & Bromwich, D. H. (2008). Development and testing of Polar Weather Research and Forecasting (WRF) Model. Part I: Greenland ice sheet meteorology. *Monthly Weather Review*, 136(6), 1971–1989.
- Holland, P. R., Corr, H. F. J., Pritchard, H. D., Vaughan, D. G., Arthern, R. J., Jenkins, A., & Tedesco, M. (2011). The air content of Larsen Ice Shelf. *Geophysical Research Letters*, 38, L10503. <https://doi.org/10.1029/2011GL047245>
- Jansen, D., Luckman, A. J., Cook, A., Bevan, S., Kulesa, B., Hubbard, B., & Holland, P. R. (2015). Brief communication: Newly developing rift in Larsen C Ice Shelf presents significant risk to stability. *The Cryosphere*, 9(3), 1223–1227. <https://doi.org/10.5194/tc-9-1223-2015>
- King, J. C., Gadian, A., Kirchgassner, A., Kuipers Munneke, P., Lachlan-Cope, T. A., Orr, A., ... Weeks, M. (2015). Validation of the summertime surface energy budget of Larsen C Ice Shelf (Antarctica) as represented in three high-resolution atmospheric models. *Journal of Geophysical Research: Atmospheres*, 120(4), 1335–1347. <https://doi.org/10.1002/2014JD022604>
- King, J. C., Lachlan-Cope, T. A., Ladkin, R. S., & Weiss, A. (2008). Airborne measurements in the stable boundary layer over the Larsen Ice Shelf, Antarctica. *Boundary-Layer Meteorology*, 127(3), 413–428. <https://doi.org/10.1007/s10546-008-9271-4>
- Kuipers Munneke, P., van den Broeke, M. R., King, J. C., Gray, T., & Reijmer, C. H. (2012). Near-surface climate and surface energy budget of Larsen C ice shelf, Antarctic Peninsula. *The Cryosphere*, 6(2), 353–363. <https://doi.org/10.5194/tc-6-353-2012>
- Luckman, A., Elvidge, A., Jansen, D., Kulesa, B., Kuipers Munneke, P., King, J., & Barrand, N. E. (2014). Surface melt and ponding on Larsen C Ice Shelf and the impact of föhn winds. *Antarctic Science*, 26(06), 625–635. <https://doi.org/10.1017/S0954102014000339>
- Marshall, G. J., Orr, A., van Lipzig, N. P. M., & King, J. C. (2006). The impact of a changing Southern Hemisphere Annular Mode on Antarctic Peninsula summer temperatures. *Journal of Climate*, 19(20), 5388–5404.
- Mayr, G. J., Armi, L., Gohm, A., Zängl, G., Durran, D. R., Flamant, C., ... Weissmann, M. (2007). Gap flows: Results from the Mesoscale Alpine Programme. *Quarterly Journal of the Royal Meteorological Society*, 133(625), 881–896. <https://doi.org/10.1002/qj.66>
- Morris, E. M., & Vaughan, D. G. (2003). Spatial and temporal variation of surface temperature on the Antarctic Peninsula and the limit of viability of ice shelves. In E. Domack et al., (Eds.), *Antarctic Peninsula climate variability: A historical and paleoenvironmental perspective* (pp. 61–68). Washington, DC: American Geophysical Union.
- Natural Environment Research Council (2014). [King, J. C.; Kirchgassner, A.; Lachlan-Cope, T.]. British Antarctic Survey Automatic Weather Station (AWS) data from the Orographic Flows and the Climate of the Antarctic Peninsula (OFCAP) project (2011), [Internet]. NCAS British Atmospheric Data Centre, 24th September 2014. <https://doi.org/10.5285/3e4cdaa3-5e89-47ae-834b-34dfee248ea4>
- Orr, A., Marshall, G. J., Hunt, J. C. R., Sommeria, J., Wang, C. G., van Lipzig, N. P. M., ... King, J. C. (2008). Characteristics of summer airflow over the Antarctic Peninsula in response to recent strengthening of westerly circumpolar winds. *Journal of the Atmospheric Sciences*, 65(4), 1396–1413.
- Powers, J. G., Manning, K. W., Bromwich, D. H., Cassano, J. J., & Cayette, A. M. (2012). A decade of Antarctic science support through AMPS. *Bulletin of the American Meteorological Society*, 93(11), 1699–1712. <https://doi.org/10.1175/bams-d-11-00186.1>
- Rignot, E., Casassa, G., Gogineni, P., Krabill, W., Rivera, A., & Thomas, R. (2004). Accelerated ice discharge from the Antarctic Peninsula following the collapse of Larsen B ice shelf. *Geophysical Research Letters*, 31, L18401. <https://doi.org/10.1029/2004GL020697>
- Scambos, T. A., Hulbe, C., Fahnestock, M., & Bohlander, J. (2000). The link between climate warming and break-up of ice shelves in the Antarctic Peninsula. *Journal of Glaciology*, 46(154), 516–530.
- Seefeldt, M. W., & Cassano, J. J. (2008). An analysis of low-level jets in the Greater Ross Ice Shelf region based on numerical simulations. *Monthly Weather Review*, 136(11), 4188–4205.
- Steinhoff, D. F., Chaudhuri, S., & Bromwich, D. H. (2009). A case study of a Ross Ice Shelf airstream event: A new perspective. *Monthly Weather Review*, 137(11), 4030–4046.

- Tedesco, M. (2009). Assessment and development of snowmelt retrieval algorithms over Antarctica from K-band spaceborne brightness temperature (1979–2008). *Remote Sensing of Environment*, 113(5), 979–997. <https://doi.org/10.1016/j.rse.2009.01.009>
- Turner, J., Colwell, S. R., Marshall, G. J., Lachlan-Cope, T. A., Carleton, A. M., Jones, P. D., ... Iagovkina, S. (2005). Antarctic climate change during the last 50 years. *International Journal of Climatology*, 25(3), 279–294. <https://doi.org/10.1002/joc.1130>
- Turner, J., Lu, H., White, I., King, J. C., Phillips, T., Hosking, J. S., ... Deb, P. (2016). Absence of 21st century warming on Antarctic Peninsula consistent with natural variability. *Nature*, 535(7612), 411–415. <https://doi.org/10.1038/nature18645>
- van den Broeke, M. (2005). Strong surface melting preceded collapse of Antarctic Peninsula ice shelf. *Geophysical Research Letters*, 32, L12815. [https://doi.org/10.1029/2005GL023247\(12\)](https://doi.org/10.1029/2005GL023247(12)).